J. Fluid Mech. (2014), *vol.* 750, *pp.* 355–371.
doi:10.1017/jfm.2014.267

Disruptive bubble behaviour leading to microstructure damage in an ultrasonic field

Tae-Hong Kim and Ho-Young Kim†

Department of Mechanical and Aerospace Engineering, Seoul National University, Seoul 151-744, Korea

(Received 26 August 2013; revised 14 February 2014; accepted 8 May 2014;
first published online 9 June 2014)

Bubble oscillations play a crucial role in ultrasonic cleaning, a process by which micro- and nanoscale contaminant particles are removed from solid surfaces, such as semiconductor wafers, photomasks and membranes. Although it is well known that the ultrasonic cleaning may damage the functional patterns of ever-shrinking size in current manufacturing technology while removing dust and debris, the mechanisms leading to such damage have been elusive. Here we report observations of the dynamics of bubbles that yield microstructure damage under a continuous ultrasonic field via high-speed imaging. We find that the bubble behaviour can be classified into four types, namely volume oscillation, shape oscillation, splitting and chaotic oscillation, depending on the acoustic pressure and bubble size. This allows us to construct a regime map that can predict the bubble behaviour near a wall based on the experimental parameters. Our visualization experiments reveal that damage of microwalls and microcantilevers arises due to either splitting small bubbles or chaotically oscillating large bubbles in the ultrasonic field, with the forces generated by them quantitatively measured.

Key words: bubble dynamics, cavitation, drops and bubbles

1. Introduction

Ultrasound travelling through a liquid produces pressure waves, which cause negative pressure during the rarefaction stage. This negative pressure may lead to cavitation from pre-existing nuclei of dissolved gas as well as the rupture of the fluid (Leighton 1994; Wagterveld *et al.* 2011). The cavitation bubbles oscillate under the continuous ultrasonic excitations, thereby generating a pressure gradient between the far-field fluid and the bubble surface (Kim *et al.* 2009). They also translate due to the primary Bjerknes force while interacting with each other through the secondary Bjerknes force (Crum 1975; Mettin *et al.* 1997). The local fluid motions induced by oscillating bubbles that undergo translation can be responsible for the cleaning of contaminant particles from solid surfaces (Kim *et al.* 2009; Gonzalez-Avila *et al.* 2011). Ultrasonic cleaning processes are widely employed for cleaning of photomasks and wafers in semiconductor industries, surgical instruments, and membranes (Lamminen, Walker & Weavers 2004). The cleaning efficiency, often measured by the particle removal efficiency (Busnaina & Gale 1997), increases

† Email address for correspondence: hyk@snu.ac.kr

with the acoustic pressure amplitude. This is because bubble mobility enhanced by high acoustic pressure leads to increased particle-detachment forces and allows a wider area to be swept by ultrasonic bubbles. However, it is well known that strong ultrasonic pressure waves lead to the damage of solid surfaces as well as the removal of contaminant particles (Holsteyns *et al.* 2005; Kim *et al.* 2010). Pits and holes on fragile substrates (Chen, Weavers & Walker 2006; Wagterveld *et al.* 2011) and broken patterns on semiconductor chips (Tomita *et al.* 2009) have been observed after ultrasonically cleaning the surfaces, but the dynamic behaviour of ultrasonic bubbles leading to such damages has been seldom captured.

Cavitation bubbles induced by electric sparks or laser pulses have been mainly used so far to investigate the interaction of bubbles with a solid wall. Unlike ultrasonic bubbles, they can be introduced into the liquid at a precisely known size and location, which greatly facilitates the experimental observation. However, the dynamics of cavitation bubbles induced under the continuous acoustic wave fields that are actually used in ultrasonic cleaning are different from those generated under the impulses from sparks or lasers. Impulsively generated cavitation bubbles are filled with vapour produced by plasma recombination and thus have a lifetime of a few microseconds (Lauterborn & Hentschel 1985). They initially expand explosively and then vanish after a few rebound cycles. Dynamic behaviour of spark- or laser-induced bubbles has been classified based on the relative size of the distance between the bubble and the solid surface and the maximum bubble radius (Shima, Takayama & Tomita 1983; Vogel, Lauterborn & Timm 1989; Lindau & Lauterborn 2003). The dents formed by such bubbles on soft substrates have been reported (Tomita & Shima 1986; Philipp & Lauterborn 1998; Brujan *et al.* 2001), revealing their disruptive capability. On the other hand, the acoustic cavitation bubbles induced under continuous waves are filled with gas dissolved in liquid, and respond periodically to driving acoustic waves with a considerably longer lifetime (Lauterborn & Ohl 1997). Because of inherent difficulties in predicting the location of individual bubbles, observations of the interaction of the ultrasonic bubbles with solid structures are scarce, in contrast to those of the spark- or laser-induced bubbles.

Therefore, here we aim to overcome the difficulties in capturing the dynamic behaviour of individual ultrasonic bubbles and analyse the interface motions and interaction with solid structures. Through the observations, we elucidate the mechanisms that result in the damage of solid structures due to ultrasonic bubbles. In the following, we first describe the experimental apparatus and technique employed in this work. We then report different types of bubble behaviours, which lead to a regime map characteristic of ultrasonic bubbles. We finally visualize the pattern-damaging process to find the disruptive mechanisms of ultrasonic bubbles that are different from those of the spark- or laser-induced bubbles.

2. Experiments

We use the apparatus shown in figure 1 to visualize the microbubble motion under continuous ultrasonic waves. The setup consists of a stainless steel bath on one side of which a piezoelectric transducer vibrating at 26 kHz is attached, an upright microscope (Olympus BX-51M) with a water immersion objective lens (Olympus LUMPLFL 10XW or 40XW), and a high-speed camera (Photron SA1.1). The high-speed camera runs at a frame rate of up to 120 kHz, which can take approximately 4–5 images of the bubble motion within a single ultrasonic period. It was ensured that the entire transient interface motion was recorded by the image

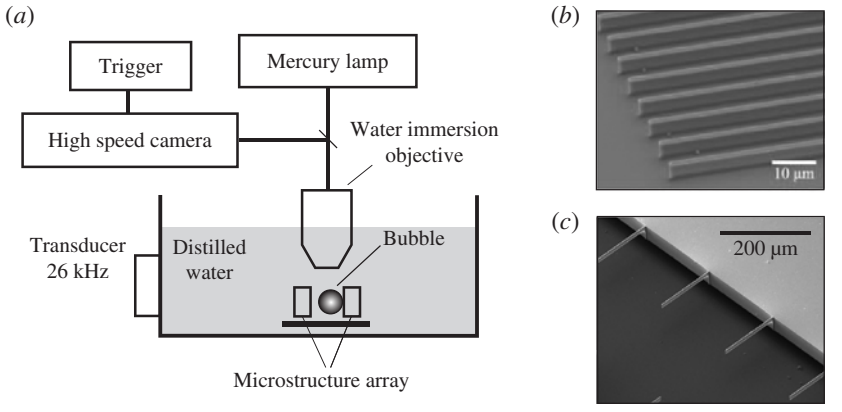

FIGURE 1. (*a*) Experimental apparatus to image the motion of ultrasonic bubbles and the micropattern-damaging processes. (*b*) SEM image of a microwall array of silicon. (*c*) SEM image of a linear array of microcantilevers of silicon.

sensor by setting the exposure time to 1/120 000 s when the frame rate was 120 kHz. That is, no matter how fast the interfacial motion may be, its trace should be captured because the camera shutter is open. Distilled water with 7 mg of O_2 per litre at room temperature as measured by an oxygen sensor (Unisense OX-100) is used as the liquid medium. For the solid walls interacting with bubbles, we use a polyimide substrate, an array of microwalls patterned on a silicon wafer, and microcantilevers. A silicon microwall array of 3.7, 2.5 and 10.6 μm in height, width and spacing, respectively, is fabricated by deep reactive ion etching. A linear array of silicon cantilever beams of 15, 130 and 3 μm in width (w), length (l) and thickness (b), respectively, is used to observe their deflections due to forces generated by bubble oscillations. Figure 1(*b*,*c*) shows scanning electron microscopy (SEM) images of the microwall array and the microcantilevers. The acoustic pressure amplitude, P_a, whose root-mean-square (r.m.s.) value can be sustained at a constant by the amplifier driving the piezoelectric transducer ranges from 35 to 76 kPa, as measured by a needle hydrophone (Precision Acoustics HPM1/1). We use the r.m.s. values of the pressure because it fluctuates naturally due to finite near-field effects, reflections from the wall, and absorption and scattering of acoustic waves by cavitation bubbles.

While the location and size of bubbles generated by a spark or laser can be precisely controlled, it is impossible to predict when and where individual bubbles will emerge and interact with a solid boundary under ultrasonic waves. Numerous cavitation bubbles that are generated ultrasonically move around rapidly due to the primary and secondary Bjerknes forces and acoustic streaming. However, we succeeded in capturing the moments individual bubbles interact with the solid wall by continually observing a selected area under the microscope until a bubble appears. Then the high-speed camera saves the images stored in the memory before and after the triggering moment. We present the visualization results of the dynamics of ultrasonic bubbles and their interaction with solid walls in the following.

3. Observations of microbubble behaviour

We start with the dynamic behaviour of a single microbubble near a rigid solid wall, a polyimide substrate in our case. In the ultrasonic field, bubbles of a wide

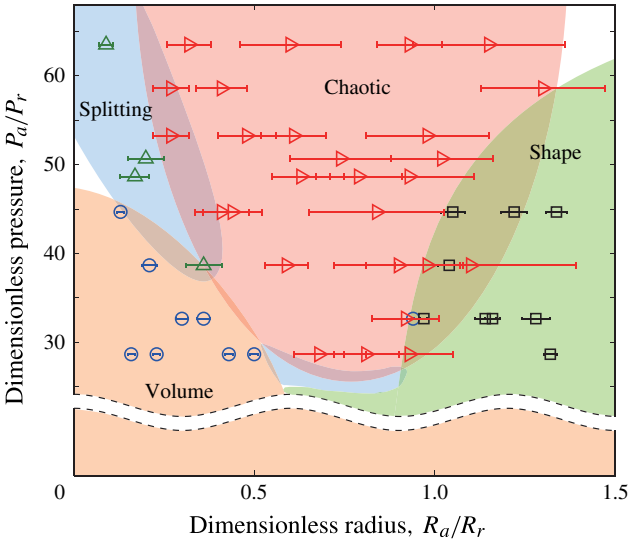

FIGURE 2. Regime map of the dynamics of cavitation bubbles in an ultrasonic field. When the bubble is no longer spherical under high-pressure-amplitude waves, we use the equivalent radius of a sphere whose area in the image is the same as that of the bubble. Error bars correspond to the standard deviations. ○, Volume oscillation; □, shape oscillation; △, splitting; ▷, chaotic oscillation.

size range are generated and oscillate. Thus, we observe how bubbles of various sizes respond to different acoustic pressure amplitudes that are controlled by the amplifier and measured by the hydrophone. These experiments allow us to construct a regime map to classify the behaviour of ultrasonic bubbles depending on the bubble size and the acoustic pressure amplitude. We find four distinct types of bubble behaviour near a solid wall, which we refer to as volume oscillation, shape oscillation, splitting, and chaotic oscillation. To find dimensionless parameters that identify the conditions in which each behaviour arises, we first consider the resonance radius of a cavitation bubble in the ultrasonic field. For a bubble undergoing harmonic radial oscillation within an inviscid liquid, the linear resonance angular frequency, ω_r, is given by the Minnaert formula (Minnaert 1933), $\omega_r = (3\kappa P_0/\rho)^{1/2}/R_r$, where κ is the adiabatic exponent (1.4 for air bubble), P_0 is the ambient pressure, ρ is the liquid density, and R_r is the nominal radius of the bubble at rest. Therefore, the resonance bubble radius corresponding to the ultrasonic frequency 26 kHz for water at $P_0 = 1$ atm is $R_r = 124$ μm. This bubble radius allows us to find the characteristic pressure of the interior of a bubble at rest with respect to the outer pressure using the Laplace formula: $P_r = 2\sigma/R_r = 1.2$ kPa, where σ is the surface tension coefficient between water and air. Using the time-averaged bubble radius scaled by the resonance radius, $\hat{R} = R_a/R_r$, and the acoustic pressure amplitude scaled by the Laplace pressure, $\hat{P} = P_a/P_r$, we obtain the regime map as shown in figure 2. Below we delineate the bubble behaviour in each regime.

At a low pressure amplitude, $\hat{P} = 29$, small bubbles with $\hat{R} < 0.5$ oscillate in radius as shown in figure 3(*a*). This volume oscillation mode occurs in the lower left region in figure 2. For very small bubbles with $\hat{R} = 0.13$, the volume oscillation is observed up to the acoustic pressure of $\hat{P} = 45$. We write the scaled magnitude of radial oscillation as $\varepsilon = (R_1 - R_2)/(2R_a)$, where R_1 and R_2 are the maximum

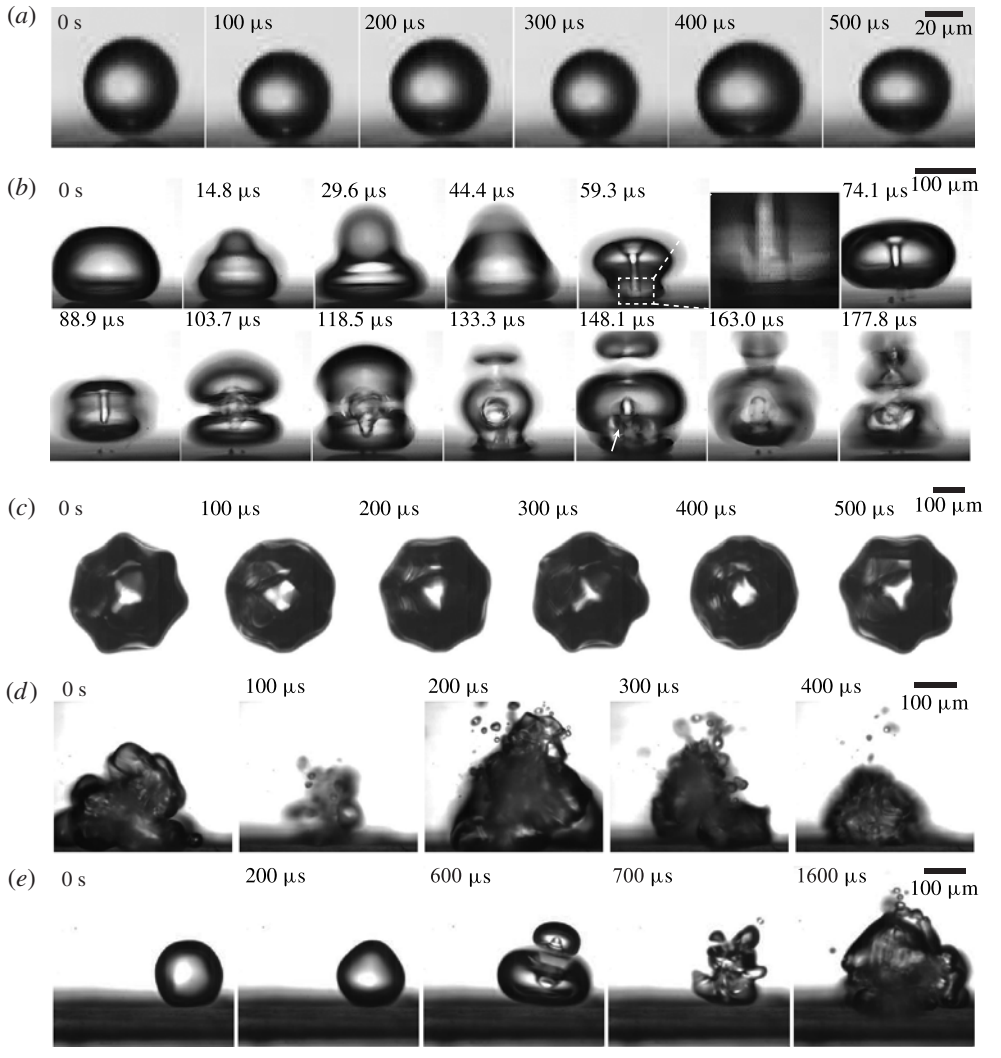

FIGURE 3. Distinct types of the dynamics of ultrasonic bubbles. (*a*) Volume oscillation of a bubble of $\hat{R} = 0.20$ at $\hat{P} = 29$. (*b*) Splitting and jetting of a bubble of $\hat{R} = 0.63$ at pressures lower than $\hat{P} = 29$. The magnified view at 59.3 μs reveals that the jet has not reached the lower interface of the bubble yet. (*c*) Shape oscillation of a bubble of $\hat{R} = 1.33$ at $\hat{P} = 45$. (*d*) Chaotic oscillation of a bubble of $\hat{R} = 1.04$ at $\hat{P} = 63$. (*e*) Evolution of the oscillation behaviour of a bubble of $\hat{R} = 0.78$ with the increase of the acoustic pressure. As $\hat{P}$ increases from zero to $\hat{P}_m$, the bubble exhibits volume oscillation (0 s), shape oscillation (200 μs), splitting (600 μs), and then chaotic oscillation (700 μs and thereafter).

and minimum radius of the bubble, respectively. At a low pressure of $\hat{P} = 29$, small bubbles with $\hat{R} = 0.16$ respond periodically with $\varepsilon = 0.12$ while ε decreases to 0.05 for large bubbles with $\hat{R} = 0.43$ and 0.5. The volume oscillation becomes stronger as the acoustic pressure increases, so that a bubble with $\hat{R} = 0.13$ vibrates in radius with $\varepsilon = 0.14$ for $\hat{P} = 45$. Further increase of the acoustic pressure qualitatively changes the response of the bubble from the volume oscillation to the splitting behaviour.

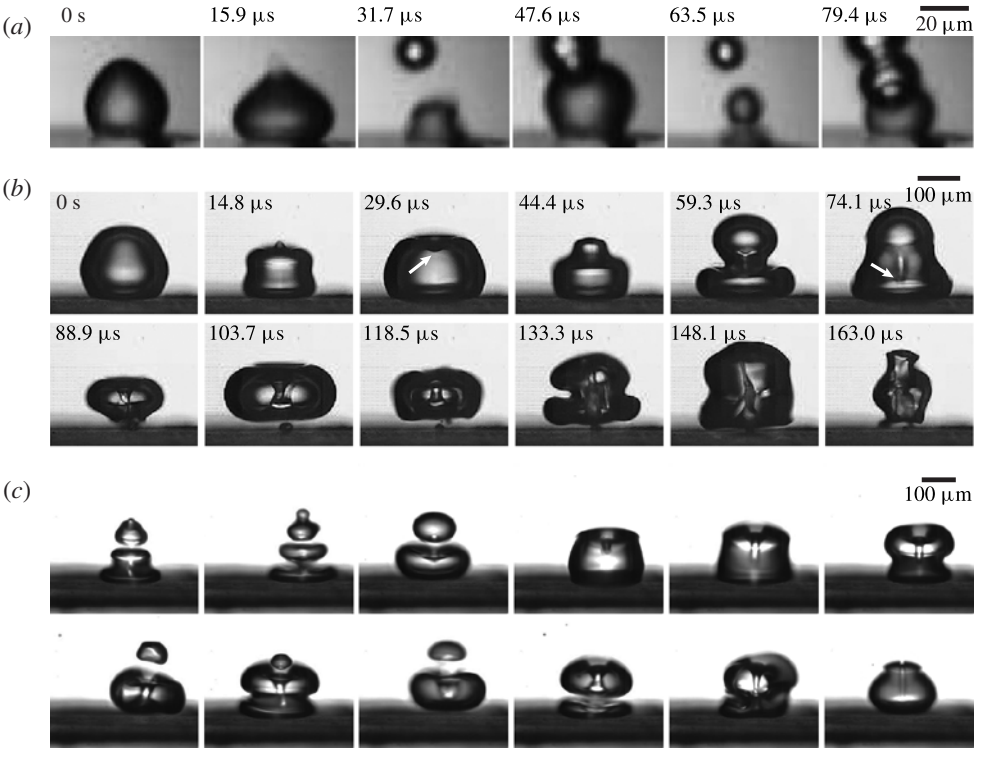

FIGURE 4. Splitting and jetting of ultrasonic bubbles. (*a*) Splitting of a small bubble of $\hat{R} = 0.13$ at $\hat{P} = 48$. (*b*) Jetting of a bubble of $\hat{R} = 0.74$ while $\hat{P}$ increases to a stable value of $\hat{P} = 29$ from zero. The dents at 29.6 and 74.1 μs, indicated by arrows, allow us to estimate the liquid jet speed. (*c*) Images of bubbles with $0.6 < \hat{R} < 0.9$ that produce liquid jets towards the wall at pressures lower than $\hat{P} = 29$.

As P_a increases, small bubbles with $\hat{R} = 0.13$ split up into two daughter bubbles as shown in figures 3(*b*) and 4. This splitting behaviour corresponds to the upper left region in figure 2. For these small bubbles, the periodic oscillation of a mode higher than the zeroth mode (volume oscillation) is seldom observed presumably because of the great difference between the excitation frequency (26 kHz) and the natural frequency for shape oscillations. For example, the Lamb frequency for the second-mode ($n = 2$) oscillation of a bubble with $\hat{R} = 0.13$ is $f_2 = (2\pi)^{-1}[(n+1)(n-1)(n+2)\sigma/(\rho R_a^3)]^{1/2} = 68$ kHz (Lamb 1932). It was reported that the threshold pressure amplitude over which the second-mode shape oscillation occurs increases with the decrease of the bubble radius (Versluis *et al.* 2010). In our experiments, the higher-mode oscillations last only a few ms, if any, before the bubbles are split, implying that the strong acoustic energy imparted to a small bubble with an increased P_a is released dominantly through the rapid breakup of bubble interfaces. Dents on both the interfaces of daughter bubbles are visible, 103.7 μs in figure 3(*b*) and 600 μs in figure 3(*e*). Upon the neck that connects the two daughter bubbles being pinched off, their interfaces are locally invaded by a liquid jet, leading to the dents (Brujan *et al.* 2001). The liquid jet following this splitting process is different from the jet observed in the spark- or laser-induced bubbles near a solid wall, which is due to asymmetric collapse of a bubble (Benjamin & Ellis 1966;

Vogel *et al.* 1989). We find that in ultrasonic bubbles, both types of liquid jet can arise: at 74.1 μs in figure 3(*b*) the liquid jet induced by asymmetric collapse of a bubble is shown, whereas the jet following the interface split is shown at 118.5 μs in figure 3(*b*) and at 600 μs in figure 3(*e*).

We use figures 3(*b*) and 4(*b*) to deduce the velocity of the jet towards the solid wall. In figure 3(*b*), assuming that the apex of the bubble at 44.4 μs travels down to the tip of the jet at 59.3 μs, the jet velocity is approximately 8.8 m s^{-1}. In figure 4(*b*), measuring the distance between the dents at 29.6 and 74.1 μs allows us to estimate the jet velocity to range from 2 to 3 m s^{-1}. Although these methods may give the lower bound of the jet speed, the values are in agreement with the previous measurements of jet speeds for ultrasonic bubbles by Crum (1979) and Prabowo & Ohl (2011). The fact that the liquid jets are frequently captured before they completely penetrate the lower interface of the bubble, 59.3 and 118.5 μs in figure 3(*b*) and 74.1 μs in figure 4(*b*), indicates that the jet speed, v_j, is unlikely to be fast enough to travel a distance equal to the bubble size within the duration of a single frame, i.e. $v_j <\sim 16.5$ m s^{-1}. The estimated jet speeds are significantly lower than the values, of the order of 100 m s^{-1}, reported for the jet induced by asymmetrical collapse of an impulsively generated bubble near a solid wall (Tomita & Shima 1986; Vogel *et al.* 1989; Philipp & Lauterborn 1998). Furthermore, Prabowo & Ohl (2011) argued that breakup of the liquid jet before its penetration of the bubble weakens the impact of the jet on the substrate. The stagnation pressure of the jet, which can be estimated as $P_s \sim (1/2)\rho v_j^2$, where v_j is the jet velocity, is of the order of 10 kPa. The viscous stress, which is scaled as $\tau \sim \mu v_j/\delta$ (Dijkink & Ohl 2008), where μ is the water viscosity and δ is the characteristic distance of the jet from the solid boundary, is of the order of 1 kPa.

Large bubbles of $\hat{R} >\sim 1$ exhibit shape oscillations as shown in figure 3(*c*) at $\hat{P} = 45$. In figure 2, the shape oscillation mode occurs in the lower right region. For large bubbles, the interface between the dense liquid and less dense gas phase is strongly accelerated into the bubble as P_a increases, so that the growth of initially small perturbations of volume oscillation leads to shape oscillation (Eller & Crum 1970; Holt & Gaitan 1996). Figure 5(*a–c*) show the shape oscillations of different sizes of bubbles. We see that the shape mode number increases with the bubble size at the fixed ultrasonic frequency, 26 kHz. Figure 5(*d*) plots the mode number versus the bubble size. The experimentally measured mode numbers of the bubbles increase almost linearly with the bubble size, but are still lower than the values predicted by Lamb's formula that is supposed to hold for bubbles oscillating in an inviscid liquid. Francescutto & Nabergoj (1978) predicted the pulsation amplitude threshold for the onset of surface waves of different mode numbers on free bubbles within a slightly viscous liquid. Although a bubble in the present experiment is close to a wall and thus requires consideration of a mirror bubble and bubble–bubble interactions for rigorous theoretical analysis, we find that the most easily excitable mode number as a function of the bubble radius is in agreement with the model of Francescutto and Nabergoj as shown in figure 5(*d*). Further study is called for to explain this agreement of the free bubble model and the experimental results of bubbles near the wall.

The shape oscillations of the bubbles become extremely violent as $\hat{P}$ increases as shown in figure 3(*d*), which we refer to as chaotic oscillation. It is characterized by ejection of multiple daughter bubbles and the consequent formation of multiple dents distributed randomly over the bubble interface as well as by irregular but vigorous distortions of the bubble interface. The chaotic regime is located in the centre of

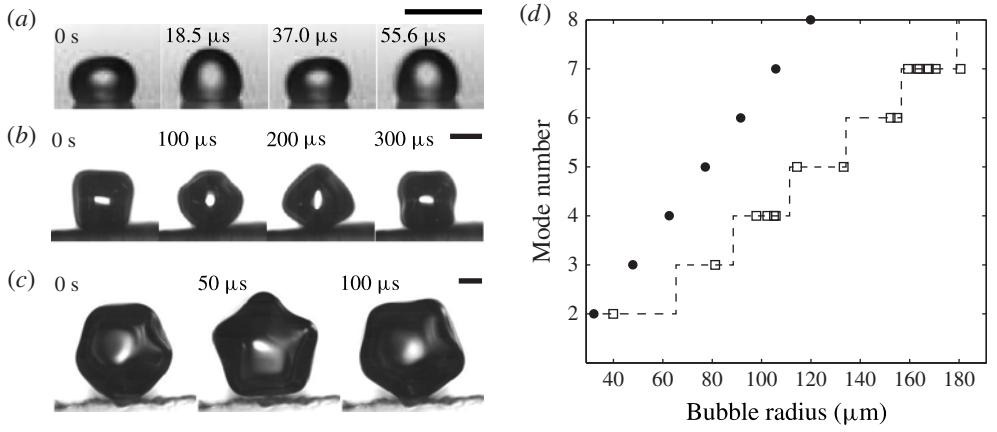

FIGURE 5. Shape oscillations of ultrasonic bubbles. (*a*) The second-mode oscillation with $\hat{R} = 0.32$ at $\hat{P} = 39$. (*b*) The fourth-mode oscillation with $\hat{R} = 0.80$ at $\hat{P} = 29$. (*c*) The fifth-mode oscillation with $\hat{R} = 1.07$ at $\hat{P} = 45$. Scale bars, 100 μm. (*d*) The mode number versus bubble radius at the acoustic forcing frequency of 26 kHz. The circles correspond to Lamb's formula, the squares to the experimental results, and the dashed line to the model of Francescutto & Nabergoj (1978).

figure 2. In this regime, the strong acoustic energy imparted to a large bubble is released by rapid motion of corrugated interfacial areas, and partly converted to surface and kinetic energy of daughter bubbles. Previous research that used high-intensity ultrasounds termed the chaotically oscillating bubble as a cloud bubble or bubble cluster, and reported emission of light or shock waves due to interaction of multiple bubbles (Lauterborn & Ohl 1997; Chen *et al.* 2009; Brujan *et al.* 2011).

Bubbles slighlty smaller than the resonance size of a freely oscillating bubble, $\hat{R} \approx 0.6$–0.9, are always found to exhibit chaotic oscillation under the stable acoustic pressure amplitude condition allowed in our setup, whose minimum is $\hat{P}_m = 29$. However, it is possible to observe the evolution of the bubble dynamics for $\hat{R} \approx 0.6$–0.9 as the acoustic pressure increases from zero to $\hat{P}_m$ upon switching the amplifier on. As shown in figure 3(*e*), the foregoing three modes of bubble behaviour, namely volume oscillation, shape oscillation and splitting, arise sequentially with the increase of the pressure amplitude. In particular, liquid jets are frequently observed for the bubbles of this size range as shown in the third frame of figures 3(*e*) and 4(*c*). In contrast, very small bubbles ($\hat{R} < 0.4$) require very strong acoustic pressure to give rise to liquid jets (Zhong *et al.* 1999; Brujan *et al.* 2011). The fact that the size range of bubbles easily prone to chaotic oscillations is shifted to values smaller than unity ($\hat{R} = 0.6$–0.9) can be explained using a formula for the resonance frequency of a bubble adjacent to a wall, f_r, as suggested by Strasberg (1953): $f_r/f_{r0} = [1 + (R/2d) - (R/2d)^4]^{-1/2}$. Here f_0 is the resonance frequency of a freely oscillating bubble, R is the nominal radius of the bubble and d is the distance of the bubble centre from the wall. The relationship implies that the presence of a wall decreases the resonance frequency of a bubble of a given radius, or equivalently, decreases the resonance radius at a given frequency because we may write $R_r/R_0 = [1 + (R/2d) - (R/2d)^4]^{-1/2}$, where R_r and R_0 are the resonance radii of a bubble near a wall and of a freely oscillating bubble, respectively (Dollet *et al.* 2008). For a bubble barely touching the wall, $R = d$, we get $R_r/R_0 \approx 0.8$,

in good agreement with the size range of bubbles easily prone to chaotic responses in figure 2.

4. Observations of micropattern-damaging processes

The damage of solid substrates due to impulsively generated bubbles has been explained by either the high-speed liquid jet directed towards the solid wall (Kornfeld & Suvorov 1944; Naudé & Ellis 1961; Benjamin & Ellis 1966) or the emission of a shock wave from the expanding bubble (Hickling & Plesset 1964; Shutler & Mesler 1965). The speed of the liquid jet induced by asymmetrical collapse of an impulsively generated bubble near a solid wall was measured to reach the order of 100 m s^{-1} as mentioned in § 3. The corresponding water hammer pressure, $P_h \sim \rho c v_j$, where c is the speed of sound in water, reaches approximately 0.1 GPa. However, the experimentally measured speed of the liquid jet formed by the splitting of ultrasonic bubbles in figure 3(*b*) is of the order of 1 m s^{-1}. Thus, the water hammer effect is negligible, lowering the possibility that the low-velocity jet of ultrasonic bubbles would damage the solid substrate. A shock wave was observed to be emitted from an impulsively generated bubble that re-expands after the collapsing phase in which the bubble content is strongly compressed (Tomita & Shima 1986; Ohl *et al.* 1999; Shaw & Spelt 2010). The pressure from the shock wave was estimated to be as high as 1 GPa (Pecha & Gompf 2000; Brujan *et al.* 2011), a value large enough to damage solid substrates (Suwito *et al.* 1999). For ultrasonic bubbles, however, such an explosive growth is unlikely because of the periodically imposed acoustic waves. In the following, we present high-speed imaging results of ultrasonic bubbles damaging micropatterns, such as microwalls and microcantilevers.

4.1. *Array of microwalls*

We first use an array of microwalls on a silicon wafer as a solid substrate to observe ultrasonic bubble damage to microstructures. Figure 6 shows the interaction of small bubbles ($\hat{R} < 0.5$) with the microstructures. Since no pattern damage arises for bubbles undergoing volume oscillations as shown in figure 6(*a*), we focus on the images of the bubbles that split due to ultrasonic waves. Figure 6(*b*) shows that the wall breaks where a microbubble splits (200 μs). An SEM image of the broken wall is also shown in figure 6(*b*). This is the first experimental evidence that splitting ultrasonic bubbles can damage microstructures, to the authors' knowledge. However, not all the splitting bubbles damage microstructures, but rather, the bubble split must occur over the microstructure to induce damage. Figure 6(*c*–*e*) shows that when the splitting bubbles are confined between the microwalls, the walls are hardly affected. Figure 6(*c*,*d*) shows that the liquid jets or pressure waves from dividing interfaces directed perpendicular to the wall surface do not break the microwalls. When the interface division is parallel to the wall, figure 6(*e*), neither the liquid jet nor the kinetic energy of the divided bubbles pushing the wall cause damage.

We now estimate the magnitude of force that leads to damage of the microwall as shown in figure 6(*b*). When a bubble lies on the microwall, the wall under the constant pressure P experiences the maximum stress at the clamped bottom, $\sigma_m = 3Ph^2/w^2$, where h and w are the height and thickness of the wall, respectively (Timoshenko & Goodier 1970). For σ_m to reach the ultimate strength of an etched single crystalline silicon substrate, $\sigma_u \sim 1$ GPa (Suwito *et al.* 1999), the pressure needs to reach 152 MPa. Since the dynamic pressure generated by the liquid jet issuing from the splitting bubble is too low (of the order of 10 kPa) as discussed

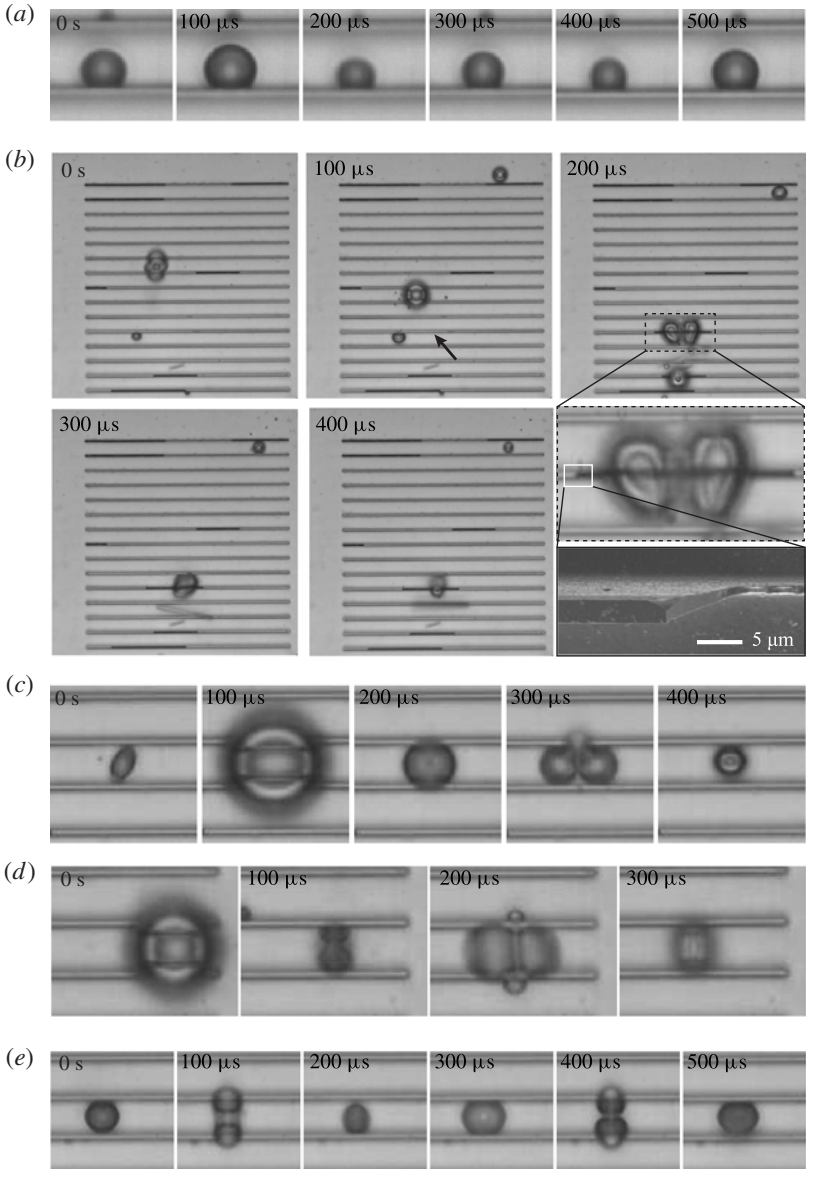

FIGURE 6. (*a*) An ultrasonic bubble undergoing volume oscillation on the silicon microwall array at $\hat{P} = 45$. (*b*) A bubble splitting on a silicon line pattern leads to its damage at $\hat{P} = 63$. The bright region indicated by an arrow at 100 μs turns dark after destruction. An SEM image of a broken microwall is also displayed. (*c*) A liquid jet from dividing interfaces is directed towards the upper wall at $\hat{P} = 63$. (*d*) Two tiny daughter bubbles are formed by splitting and a liquid column perpendicular to both the walls is visible at $\hat{P} = 63$. (*e*) Periodic splitting of bubbles that form interfaces parallel to the walls at $\hat{P} = 63$.

in § 3, we are naturally led to assume that such a high pressure is caused by the shock emitted from the splitting interface. The impulsive pressure due to the shock wave from a splitting spark-induced bubble confined within a narrow gap between

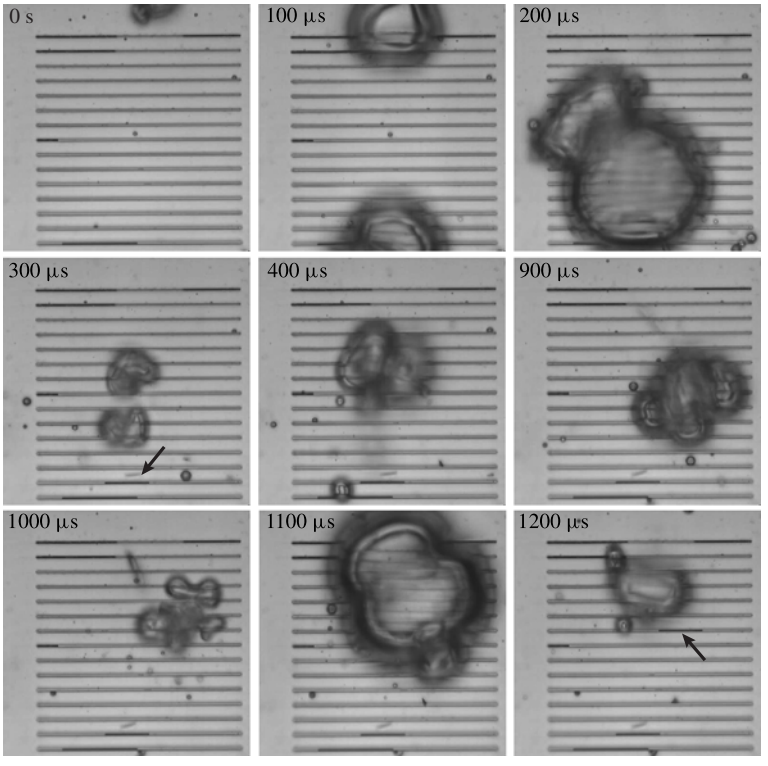

FIGURE 7. Destruction of microwalls due to chaotically oscillating bubbles at $\hat{P} = 63$. The arrows indicate the regions where destruction has occurred.

flat plates was shown to damage solid structures by Ishida *et al.* (2001). The pressure exerted on the microwall due to the shock is estimated as a water hammer pressure, $P_h \sim \rho v_s c$, where v_s is the velocity of a liquid flow stemming from bubble split. For P_h to reach 152 MPa, v_s would be 100 m s^{-1}. Taking this velocity as a characteristic splitting speed of a 100 μm radius bubble, it takes only 1 μs for the split to occur, meaning that even a high-speed camera running at 10^6 frames per second (f.p.s.) cannot resolve the splitting process.

Figure 7 shows the damaging effects of chaotically oscillating bubbles on the microwall arrays. The shapes of the bubbles change drastically in each frame, is taken every 100 μs, demonstrating the chaotic and vigorous nature of this type of oscillation. We clearly see that the sections of microwalls indicated by arrows in the figure become dark after being broken by the bubble. However, the extremely fast and unpredictable bubble behaviour imaged by the high-speed camera running only at 10 000 f.p.s. makes it difficult to gain physical insight into how the chaotically oscillating bubble generates forces strong enough to break microstructures. Hence, we use an array of microcantilevers to measure the forces in the following.

4.2. *Array of microcantilevers*

To measure the forces generated by oscillating bubbles quantitatively, we use an array of silicon microcantilevers as shown in figure 1(*c*), which are deflected by oscillating bubbles as illustrated in figure 8(*a*). We first confirmed that the deflection of the

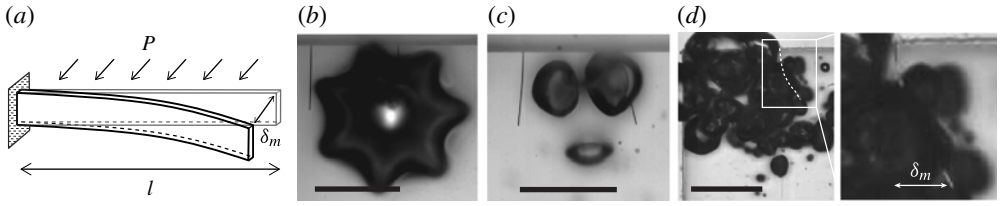

FIGURE 8. Deflection of microcantilevers due to ultrasonic bubbles at $P_a = 76$ kPa. (*a*) Schematic model, (*b*) shape oscillation, (*c*) splitting, (*d*) chaotic oscillation. The white dashed line has been drawn to aid identification of the microcantilever. Scale bars, 200 μm.

Type	δ_m (μm)	P (kPa)	v_d (m s^{-1})	v_h (m s^{-1})
Shape oscillation	2.6	26	5.1	0.02
Splitting	30.5	308	17.5	0.22
Chaotic oscillation	57.0	575	24.0	0.40

TABLE 1. Measurement results of the deflection of the free end of cantilevers, δ_m, and the corresponding bubble pressure P in each oscillation mode at the constant acoustic pressure condition of $\hat{P} = 63$. We also list the characteristic velocities of liquid flows, v_d and v_h, assuming that the deflection is due to dynamic pressure and water hammer, respectively: $v_d = (P/\rho)^{1/2}$ and $v_h = P/\rho c$.

cantilevers due to acoustic streaming and pressure fluctuations in the ultrasonic field is negligible by measuring the deflections in the absence of adjacent bubbles. The resonance frequency of a silicon cantilever of $[w, l, b] = [15, 130, 3]$ μm in vacuum, $f_0 = b(E/\rho_c)^{1/2}/(4\pi l^2) = 117$ kHz, and that in water, $f_w = f_0[1 + \pi\rho w/(4\rho_c b)]^{-1/2} = 70$ kHz (Sader 1998), thus the resonance frequencies are far from the external ultrasonic frequency. Here $E = 160$ GPa and $\rho_c = 2330$ kg m^{-3} are Young's modulus and the density of the cantilever, respectively. We note that the cantilevers situated near the oscillating bubble may influence the motions and forces of the bubble, and the bubble motion may in turn affect the cantilever vibration. Such coupling may yield differences in bubble forces compared to those estimated in § 4.1. However, its effects are expected to be weak because of the significant difference between f_w and the ultrasonic frequency and the relatively small beam width (15 μm) compared to bubble size. When shape and chaotic oscillations arise, the bubble diameter is significantly larger than the beam length as shown in figure 8(*b*,*d*), further reducing the effects of the coupling.

Assuming that the cantilever is subjected to uniform pressure P arising from the bubble oscillation, the maximum displacement occurring at the free end is given by $\delta_m = 3Pl^4/(2Eb^3)$. The characteristic pressure P corresponds to the bubble pressure in figure 8(*b*,*d*), and to a representative pressure taking into account the bubble pressure exerted over 73 % of the cantilever beam length from the anchor and the pressure due to liquid flow over the remaining part of the beam near the free end in figure 8(*c*). We find large differences in δ_m depending on the bubble oscillation mode even at the same acoustic pressure amplitude: different modes are selected by different bubble sizes. Table 1 lists the measurement results of δ_m and the corresponding pressure P for each oscillation mode. In the table, δ_m for the shape oscillation and splitting modes

corresponds to the maximum deflection observed, and that for the chaotic oscillation is the maximum deflection imaged before destruction.

The shape oscillation as shown in figure 8(*b*) is measured to exert the weakest pressure of the three oscillation modes, 26 kPa, on the cantilever. Taking the characteristic oscillation velocity of the bubble interface, $U \sim \varepsilon\omega R_a \sim \varepsilon\omega R_r\hat{R}$, the characteristic magnitude of dynamic pressure associated with the periodic oscillation of a bubble is scaled as $P_d \sim \rho U^2 \sim \rho\varepsilon^2\omega^2 R_r^2\hat{R}^2$. For shape oscillations, $\varepsilon \sim 10^{-1}$, leading to $U \sim 1$ m s^{-1} and $P_d \sim 10$ kPa, which is consistent with the measurement results in table 1. Assuming that the pressure of the shape oscillation, $P = 26$ kPa, is due to water hammer, the liquid velocity is estimated to be 0.02 m s^{-1}, which is too low compared to our experimental observations and unlikely to lead to water hammering. If we take $\hat{R} \approx 0.5$ and $\varepsilon \approx 1$ for the splitting mode, and $\hat{R} \approx 1$ and $\varepsilon \approx 1$ for the chaotic oscillation mode, then the dynamic pressure for both modes is scaled as $P_d \sim 10^2$ kPa, in agreement with the experimental values in table 1. On the other hand, the liquid velocities assuming the water hammer effect, $v_h = 0.22$ and 0.40 m s^{-1} for splitting and chaotic oscillation, respectively, are too low to yield significant water hammer effects. Therefore, the measured pressure values in table 1 correspond to the strength of the dynamic pressure effect not water hammer.

The bubble pressure that can cause the stress at the clamped end of the cantilever to reach the ultimate strength of an etched single crystalline silicon substrate (∼1 GPa), $P \sim \sigma_u b^2/(3l^2)$ (Timoshenko & Goodier 1970), is estimated to be $\sim 10^2$ kPa, a value comparable to the pressure of splitting and chaotically oscillating bubbles in table 1. We indeed see that microcantilevers are broken by extremely violent motions of chaotically oscillating bubbles in figure 9. Although dynamic pressure arising from the chaotic oscillation of a bubble, of the order of 10^2 kPa, is strong enough to break the microcantilever, it is still lower than the pressure needed to break the microwalls ($\sim 10^2$ MPa). This estimate again confirms that the shock effects should come into play to damage the microwalls. Just as a small bubble splitting into two can generate shocks as discussed in § 4.1, splitting of multiple bubbles, a typical process in chaotic oscillation, can emit shock waves. Also, secondary shocks due to interaction of the shock and a cloud of bubble can contribute to microstructure damage (Brujan *et al.* 2011). These high-speed processes leading to emission of shocks that eventually break microstructures like the walls in figure 7 cannot be resolved with the present high-speed camera. The shock waves from a cloud of bubbles were captured using a shadowgraph method by Brujan *et al.* (2011).

We have shown that while microwalls can be broken only by the shock effects of bubble splitting and chaotic oscillation, microcantilevers can be damaged by the dynamic-pressure effects of violently oscillating bubbles. Since the aspect ratio of nanopatterns of integrated-circuit chips steadily increases with the ever-shrinking thickness of the patterns in the current semiconductor manufacturing technology (Wu, Kumar & Pamarthy 2010), the possibility that the dynamic-pressure effects of splitting and chaotically oscillating bubbles may damage nanopatterns grows. Here we estimate the critical aspect ratio of cylindrical pillars, frequently used for nanoelectronic devices including supercapacitors (Chang *et al.* 2010) and solar cells (Garnett & Yang 2010), which can be broken by dynamic-pressure effects. The maximum stress occurring at the clamped end under the uniform loading of pressure P is given by $\sigma_m = (16/\pi)(h/a)^2 P$ (Timoshenko & Goodier 1970), where a is the pillar diameter. Figure 10 plots σ_m versus the aspect ratio h/a assuming that P is in the range 100 and 900 kPa. It shows that high-aspect-ratio nanopillars adopted in current nanoelectronic chips with h/a exceeding 20 (Henry *et al.* 2009) can be damaged by the dynamic-pressure effects of violently oscillating microbubbles.

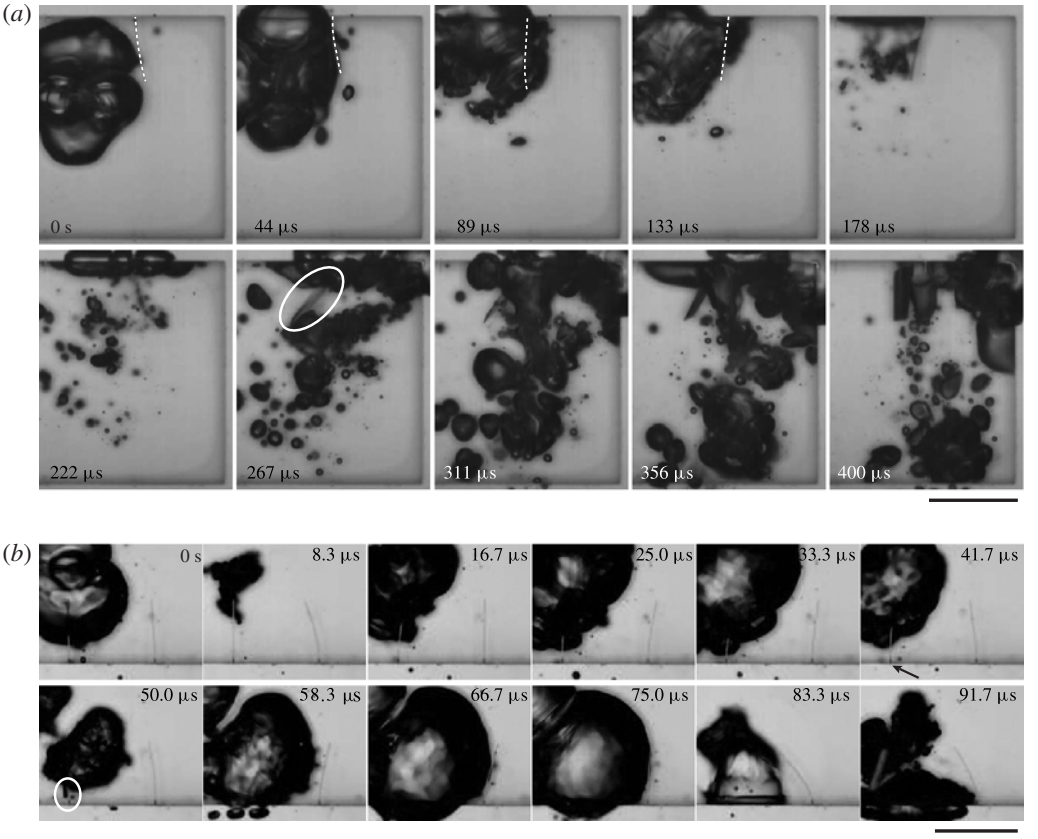

FIGURE 9. High-speed images of a chaotically oscillating bubble breaking a silicon microcantilever. (*a*) The chaotic oscillation can be extremely violent leading to the cantilever fracture. The white dashed lines have been drawn to aid identification of the microcantilever. A fragment is shown at 267 μs enclosed by an ellipse. (*b*) The microcantilever indicated by an arrow disappears between the images at 41.7 μs and 50.0 μs. The fragment is shown at 50.0 μs enclosed by an ellipse. Scale bars, 200 μm.

5. Conclusions

In summary, we have constructed a regime map of bubble behaviour under ultrasonic vibrations identifying the parameter ranges that result in the four distinct oscillation types: volume oscillation, shape oscillation, splitting and chaotic oscillation. Also, we have captured the dynamic processes of microstructure damage due to ultrasonic bubbles, which have rarely been available so far. Our experimental results indicate that liquid jets following the asymmetric collapse of a bubble near a solid wall, which have been frequently assumed to be responsible for solid damage based on the observations made with impulsively generated bubbles, have negligible effects on the microstructures in an ultrasonic field. Rather, damage of microwalls and microcantilevers has been found to occur due to either small bubbles undergoing splitting or large bubbles exhibiting chaotic oscillations. In particular, we have shown that dynamic pressure exerted by violently oscillating bubbles is capable of damaging high-aspect-ratio structures like cantilevers and pillars. To enable the application of the ultrasonic cleaning process in manufacturing of semiconductor chips with

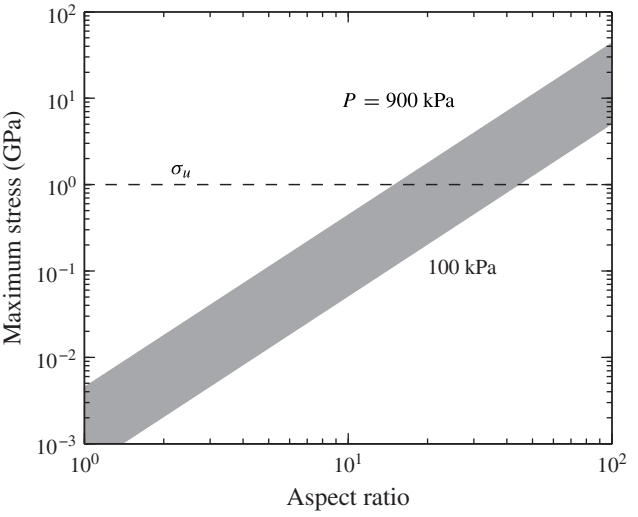

FIGURE 10. Maximum stress at the clamped end of a cylindrical silicon pillar due to the uniform pressure P exerted by microbubbles as a function of the aspect ratio, h/a.

extremely fragile nanopatterns of ever-shrinking sizes, the ultrasonic frequency and amplitude should be carefully tuned to minimize the splitting and chaotic oscillation of microbubbles.

This work could be a starting point for a complete understanding of the disruptive behaviour of microbubbles in an ultrasonic field, although we have to wait until the high-speed imaging technique catches up with the bubble oscillation speed to acquire detailed, time-resolved information on violent bubble motion. In addition, our experimental findings can help to extend the applications of vigorous bubble oscillations to cleaning of membranes (Lamminen *et al.* 2004; Chen *et al.* 2006) and even clothes (Gallego-Juarez *et al.* 2010). Surface modification of metal surfaces for wettability control can also benefit from vigorous bubble oscillations that selectively damage the surface and lead to tailored surface roughness (Belova *et al.* 2011).

Acknowledgement

This work was supported by the National Research Foundation of Korea (Grant Nos. 2013034978 and 2013055323) via SNU-IAMD.

REFERENCES

BELOVA, V., GORIN, D. A., SHCHUKIN, D. G. & MÖHWALD, H. 2011 Controlled effect of ultrasonic cavitation on hydrophobic/hydrophilic surface. *ACS Appl. Mater. Interfaces* **3**, 417–425.

BENJAMIN, T. B. & ELLIS, A. T. 1966 The collapse of cavitation bubbles and the pressures thereby produced against solid boundaries. *Phil. Trans. R. Soc. Lond.* A **260**, 221–240.

BRUJAN, E. A., IKEDA, T., YOSHINAKA, K. & MATSUMOTO, Y. 2011 The final stage of the collapse of a cloud of bubbles close to a rigid boundary. *Ultrason. Sonochem.* **18**, 59–64.

BRUJAN, E. A., NAHEN, K., SCHMIDT, P. & VOGEL, A. 2001 Dynamics of laser-induced cavitation bubbles near an elastic boundary. *J. Fluid Mech.* **433**, 251–281.

BUSNAINA, A. A. & GALE, G. W. 1997 Removal of silica particles from silicon substrates using megasonic cleaning. *Particul. Sci. Technol.* **15**, 361–369.

CHANG, S.-W., OH, J., BOLES, S. T. & THOMPSON, C. V. 2010 Fabrication of silicon nanopillar-based nanocapacitor arrays. *Appl. Phys. Lett.* **96**, 153108.

CHEN, D., WEAVERS, L. K. & WALKER, H. W. 2006 Ultrasonic control of ceramic membrane fouling by particles: effect of ultrasonic factors. *Ultrason. Sonochem.* **13**, 379–387.

CHEN, H., LI, X., WAN, M. & WANG, S. 2009 High-speed observation of cavitation bubble clouds near a tissue boundary in high-intensity focused ultrasound fields. *Ultrasonics* **49**, 289–292.

CRUM, L. A. 1975 Bjerknes forces on bubbles in a stationary sound field. *J. Acoust. Soc. Am.* **57**, 1363–1370.

CRUM, L. A. 1979 Surface oscillations and jet development in pulsating bubble. *J. Phys. Colloq.* **40**, 285–288.

DIJKINK, R. & OHL, C.-D. 2008 Measurement of cavitation induced wall shear stress. *Appl. Phys. Lett.* **93**, 254107.

DOLLET, B., VAN DER MEER, S. M., GARBIN, V. & DE JONG, N. 2008 Nonspherical oscillations of ultrasound contrast agent microbubbles. *Ultrasound Med. Biol.* **34**, 1465–1473.

ELLER, A. I. & CRUM, L. A. 1970 Instability of the motion of a pulsating bubble in a sound field. *J. Acoust. Soc. Am.* **47**, 762–767.

FRANCESCUTTO, A. & NABERGOJ, R. 1978 Pulsation amplitude threshold for surface waves on oscillating bubbles. *Acta Acust. United Ac.* **41**, 215–220.

GALLEGO-JUAREZ, J. A., RIERA, E., ACOSTA, V., RODRÍGUEZ, G. & BLANCO, A. 2010 Ultrasonic system for continuous washing of textiles in liquid layers. *Ultrason. Sonochem.* **17**, 234–238.

GARNETT, E. & YANG, P. 2010 Light trapping in silicon nanowire solar cells. *Nano Lett.* **10**, 1082–1087.

GONZALEZ-AVILA, S. R., HUANG, X., QUINTO-SU, P. A., WU, T. & OHL, C.-D. 2011 Motion of micrometer sized spherical particles exposed to a transient radial flow: attraction, repulsion, and rotation. *Phys. Rev. Lett.* **107**, 074503.

HENRY, M. D., WALAVALKAR, S., HOMYK, A. & SCHERER, A. 2009 Alumina etch masks for fabrication of high-aspect-ratio silicon micropillars and nanopillars. *Nanotechnology* **20**, 255305.

HICKLING, R. & PLESSET, M. S. 1964 Collapse and rebound of a spherical bubble in water. *Phys. Fluids* **7**, 7–14.

HOLSTEYNS, F., LEE, K., GRAF, S., PALMANS, R., VEREECKE, G. & MERTENS, P. W. 2005 Megasonics: a cavitation driven process. *Solid State Phenom.* **103–104**, 159–162.

HOLT, R. G. & GAITAN, D. F. 1996 Observation of stability boundaries in the parameter space of single bubble sonoluminescence. *Phys. Rev. Lett.* **77**, 3791–3794.

ISHIDA, H., NUNTADUSIT, C., KIMOTO, H., NAKAGAWA, T. & YAMAMOTO, T. 2001 Cavitation bubble behavior near solid boundaries. In *Proceedings CAV2001 Fourth International Symposium on Cavitation, California Institute of Technology, Pasadena, CA*.

KIM, W., KIM, T.-H., CHOI, J. & KIM, H.-Y. 2009 Mechanism of particle removal by megasonic waves. *Appl. Phys. Lett.* **94**, 081908.

KIM, W., PARK, K., OH, J., CHOI, J. & KIM, H.-Y. 2010 Visualization and minimization of disruptive bubble behavior in ultrasonic field. *Utrasonics* **50**, 798–802.

KORNFELD, M. & SUVOROV, L. 1944 On the destructive action of cavitation. *J. Appl. Phys.* **15**, 495–506.

LAMB, H. 1932 *Hydrodynamics*. Cambridge University Press.

LAMMINEN, M. O., WALKER, H. W. & WEAVERS, L. K. 2004 Mechanisms and factors influencing the ultrasonic cleaning of particle-fouled ceramic membranes. *J. Membr. Sci.* **273**, 213–223.

LAUTERBORN, W. & HENTSCHEL, W. 1985 Cavitation bubble dynamics studied by high-speed photography and holography: part one. *Ultrasonics* **23**, 260–268.

LAUTERBORN, W. & OHL, C.-D. 1997 Cavitation bubble dynamics. *Ultrason. Sonochem.* **4**, 65–75.

LEIGHTON, T. G. 1994 *The Acoustic Bubble*. Academic.

LINDAU, O. & LAUTERBORN, W. 2003 Cinematographic observation of the collapse and rebound of a laser-produced cavitation bubble near a wall. *J. Fluid Mech.* **479**, 327–348.

METTIN, R., AKHATOV, I., PARLITZ, U., OHL, C. D. & LAUTERBORN, W. 1997 Bjerknes forces between small cavitation bubbles in a strong acoustic field. *Phys. Rev.* E **56**, 2924–2931.

MINNAERT, M. 1933 On musical air bubbles and the sounds of running water. *Phil. Mag.* **16**, 235–248.

NAUDÉ, C. F. & ELLIS, A. T. 1961 On the mechanism of cavitation damage by nonhemispherical cavities in contact with a solid boundary. *Trans. ASME D: J. Basic Engng* **83**, 648–656.

OHL, C.-D., KURZ, T., GEISLER, R., LINDAU, O. & LAUTERBORN, W. 1999 Bubble dynamic, shock waves and sonoluminescence. *Phil. Trans. R. Soc. Lond.* A **357**, 269–294.

PECHA, R. & GOMPF, B. 2000 Microimplosions: cavitation collapse and shock wave emission on a nanosecond time scale. *Phys. Rev. Lett.* **84**, 1328–1330.

PHILIPP, A. & LAUTERBORN, W. 1998 Cavitation erosion by single laser-produced bubbles. *J. Fluid Mech.* **361**, 75–116.

PRABOWO, F. & OHL, C.-D. 2011 Surface oscillation and jetting from surface attached acoustic driven bubbles. *Utrason. Sonochem.* **18**, 431–435.

SADER, J. E. 1998 Frequency response of cantilever beams immersed in viscous fluids with applications to the atomic force microscope. *J. Appl. Phys.* **84**, 64–76.

SHAW, S. J. & SPELT, P. D. M. 2010 Shock emssion from collapsing gas bubbles. *J. Fluid Mech.* **646**, 363–373.

SHIMA, A., TAKAYAMA, K. & TOMITA, Y. 1983 Mechanism of impact pressure generation from spark-generated bubble collapse near a wall. *AIAA J.* **21**, 55–59.

SHUTLER, N. D. & MESLER, R. B. 1965 A photographic study of the dynamics and damage capabilities of bubbles collapsing near solid boundaries. *Trans. ASME D: J. Basic Engng* **87**, 648–656.

STRASBERG, M. 1953 The pulsation frequency of nonspherical gas bubbles in liquids. *J. Acoust. Soc. Am.* **25**, 536–537.

SUWITO, W., DUNN, M. L., CUNNINGHAM, S. J. & READ, D. T. 1999 Elastic moduli, strength, and fracture initiation at sharp notches in etched single crystal silicon microstructure. *J. Appl. Phys.* **85**, 3519–3534.

TIMOSHENKO, S. P. & GOODIER, J. N. 1970 *Theory of Elasticity*. McGraw-Hill.

TOMITA, H., INUKAI, M., UMEZAWA, K. & JI, L. 2009 Direct observation of single bubble cavitation damage for MHz cleaning. *Solid State Phenom.* **145–146**, 3–6.

TOMITA, Y. & SHIMA, A. 1986 Mechanism of implusive pressure generation and damage pit formation by bubble collapse. *J. Fluid Mech.* **169**, 535–564.

VERSLUIS, M., GOERTZ, D. E., PALANCHON, P., HEITMAN, I. L., VAN DER MEER, S. M., DOLLET, B., DE JONG, N. & LOHSE, D. 2010 Microbubble shape oscillations excited through ultrasonic parametric driving. *Phys. Rev.* E **82**, 026321.

VOGEL, A., LAUTERBORN, W. & TIMM, R. 1989 Optical and acoustic investigations of the dynamics of laser-produced cavitation bubbles near a solid boundary. *J. Fluid Mech.* **206**, 299–338.

WAGTERVELD, R. M., BOELS, L., MAYER, M. J. & WITKAMP, G. J. 2011 Visualization of acoustic cavitation effects on suspended calcite crystal. *Ultrason. Sonochem.* **18**, 216–225.

WU, B., KUMAR, A. & PAMARTHY, S. 2010 High-aspect-ratio silicon etch: a review. *J. Appl. Phys.* **108**, 051101.

ZHONG, P., LIN, H., XI, X., ZHU, S. & BHOGTE, E. S. 1999 Shock wave-inertial microbubble interaction: methodology, physical characterization, and bioeffect study. *J. Acoust. Soc. Am.* **105**, 1997–2009.